

Article

A Case Study on Microphysical Characteristics of Mesoscale Convective System Using Generalized DSD Parameters Retrieved from Dual-Polarimetric Radar Observations

Soohyun Kwon ¹, Sung-Hwa Jung ¹ and GyuWon Lee ^{2,*}

¹ Weather Radar Center, Korea Meteorological Administration, Seoul 07062, Korea; soohyun03@korea.kr (S.K.); shjung95@korea.kr (S.-H.J.)

² Department of Astronomy and Atmospheric Sciences, Center for Atmospheric Remote Sensing (CARE), Kyungpook National University, Daegu 41566, Korea

* Correspondence: gyuwon@knu.ac.kr; Tel.: +82-53-950-6361

Received: 5 April 2020; Accepted: 26 May 2020; Published: 3 June 2020



Abstract: The microphysical characteristics of a mesoscale convective system (MCS) during a summer monsoon of South Korea are investigated using the generalized drop size distributions (DSD) that are derived from S-band dual-polarization radar data. The characteristics parameters of generalized DSDs (generalized number concentration, N_0' and generalized mean diameter, D_m) are directly calculated from DSD's two moments without any assumption on the DSD model. Relationships between Z_{DR} and generalized DSD parameters normalized by Z_H are derived in the form of the polynomial equation. Verification of the retrieved DSD parameters is conducted with the 2-D video disdrometer (2DVD) located about 23 km from the radar. The standard deviations (SD) of retrieved DSD parameters are about 0.26 for $\log N_0'$, and about 0.11 for D_m because of the variability of DSDs. The SD of the retrieved $\log N_0'$ from the dual-polarimetric measurement reaches to about 0.46 (almost double) for 11 rain events while the accuracy of retrieved D_m is quite higher (~ 0.19). This higher error in retrieved $\log N_0'$ is likely attributed to the larger discrepancy in radar-observed and DSD-calculated Z_{DR} when Z_H is low. This retrieval technique is applied to a mesoscale convective system (MCS) case to investigate the Lagrangian characteristics of the microphysical process. The MCS is classified into the leading edge and trailing stratiform region by using the storm classification algorithm. The leading edge dominated by strong updraft showed the broad DSD spectra with a steady temporal increase of D_m throughout the event, likely because of the dominant drop growth by the collision-coalescence process. On the other hand, the drop growth is less significant in the trailing stratiform region as shown by the nearly constant D_m for the entire period. The DSD variation is also controlled by the new generation of drops in the leading edge and less extent in the trailing stratiform during the early period when precipitation systems grow. When the system weakens, the characteristic number concentration decreases with time, indicating the new generation of drops becomes less significant in both regions.

Keywords: drop size distribution; S-band dual-polarization radar; microphysics; DSD retrieval; mesoscale convective system

1. Introduction

Drop size distribution (DSD) is an outcome of the complex microphysical processes of precipitation particles (e.g., collision-coalescence, break-up, evaporation, etc.). The exponential DSD, $N(D) = N_0 \exp(-\Lambda D)$, has some limitations to describe these processes with fixed

N_0 ($=8000 \text{ m}^{-3}\text{mm}^{-1}$) and varying slope Λ [1]. The normalized form of DSD describes these physical processes of DSD and variation of DSD [2]. Ref. [3] found that the generalized DSD function based on the two moments scaling law is immune to the shape of DSD spectra and only depends on the generalized intercept parameters (N_0') and generalized diameter parameters (D_m').

The parameters of DSD function have been retrieved with polarimetric radar observations using the constrained relationship, neural-network algorithm, Bayesian theorem, and variational method [4–9]. The constrained-gamma method [9] and the β method [6] are widely used to retrieve the DSD parameters. Three governing parameters of gamma DSD function (N_0 , μ , and Λ) are calculated from an empirical relationship between the shape (μ) and slope (Λ) parameters and from Z_H and Z_{DR} . Ref. [10] found that β (the slope of the raindrop shape-size relationship) is sufficiently sensitive to dual-polarization measurement. The DSD parameters (D_0 , N_W , μ) are represented using β calculated from dual-polarization parameters [6]. The β method shows that the noise of K_{DP} at weak radar echo is transferred to the retrieved DSD parameters [11]. The constrained-gamma method provides relatively reasonable DSD parameters for a broad range of DSDs. However, several issues (e.g., natural DSD variability, sampling error) remain in the constrained-gamma method [12]. In this study, we neglected the significant change of the shape of normalized DSDs and assumed the two parameters (N_0' and D_m') contain the most discernible variation of DSDs. This resulted in no predefined empirical relationship between μ and Λ parameters in the retrieval equation.

Spatial and temporal variations of microphysical properties in precipitation systems are analyzed with the retrieved DSD parameters [11–15]. The variation of DSDs according to climate regions and precipitation systems is also investigated [13]. Ref. [11] analyzed the microphysical characteristics for three precipitation systems using DSD parameters derived from the constrained-gamma method. They show that the largest D_0 and high number concentration are characterized at the regions of the updrafts prevailed, and relatively high Z_H and low Z_{DR} were found in the downdraft region. Mesoscale convective systems cause heavy precipitation and resulting in severe damage because of their long-lived lifetime and well-organized structure [14,15]. A squall line, in particular, contains a distinctive structure: the leading edge and trailing wide stratiform region that should have distinctive microphysical evolution [14,15]. The microphysical process of the squall lines was investigated by disdrometric measurements [14,15] and radar retrieved DSDs [12,13] mostly in the Eulerian framework. We have selected a squall line case to investigate the different microphysical processes within a precipitation system in the Lagrangian framework without any assumption on the shape of DSDs.

In this study, we retrieved the generalized characteristic DSD parameters, D_m' and N_0' , [3] of double-moments scaling normalized DSD function. Relationships between dual-polarization parameters and generalized characteristic DSD parameters are derived with disdrometer measurements. The retrieved generalized DSD parameters are evaluated with a two-dimensional video disdrometer (2DVD). The derived relationships are utilized to retrieve the microphysical parameters from the dual-polarimetric radar, and their retrieval accuracy is evaluated. Furthermore, the microphysical characteristics of a mesoscale convective system (MCS) are investigated in the Lagrangian frame and a statistical manner.

2. Data

The DSDs collected from a 2DVD at Jinchun Weather Observatory operated by Korea Meteorological Administration (KMA) are used to derive the empirical relationship between polarimetric radar variables and microphysical parameters (Figure 1). These derived relationships are used to retrieve microphysical parameters from S-band dual-polarimetric radar at Bisl Mountain (BSL radar, Figure 1). For the validation of the retrieved microphysical parameters, DSDs observed from 2DVD at the main campus of Kyungpook National University that is 23 km away from the northwest of BSL radar is utilized. The BSL radar is located at the top of the mountain Bisl (1085 m altitude) and routinely observes a volume scan every 2.5 min with 6 plan position indicators (PPIs) at elevation angles of -0.5° , 0.0° , 0.5° , 0.8° , 1.2° , 1.6° . The first “negative” and 0.0° elevation angles are

not common to the operational radars. However, this radar is installed solely for flood forecasting and requires measurements near the surface with a rapid update, requiring such elevation angles. The use of these angles requires careful elimination of ground clutter. A PPI has a resolution of $125\text{ m} \times 1^\circ$ in radial and azimuthal directions and observes up to 150 km (Table 1).

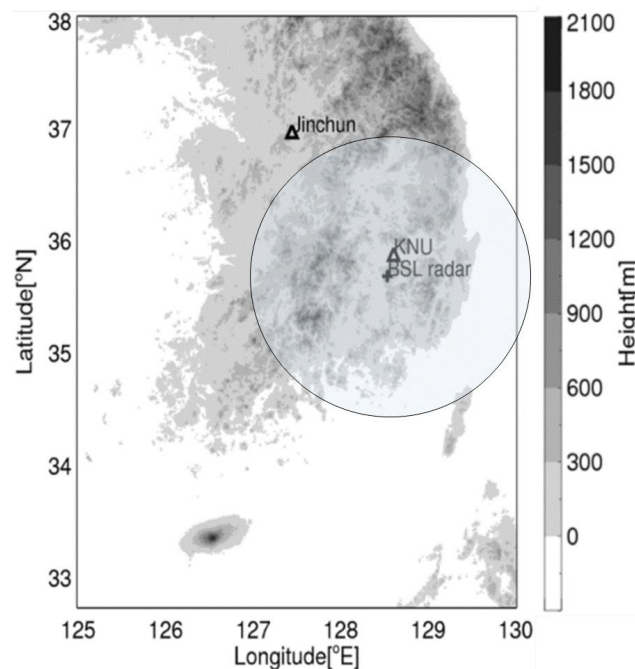


Figure 1. Deployment of two 2-D video disdrometers (2DVDs) at Jinchun and KNU sites and S-band dual-polarization radar in the Korean Peninsula. The symbols of the triangle (Δ) indicate the location of 2DVDs. The symbol of the plus (+) represents the S-band dual-polarization radar at the top of Mt. Bisul (BSL radar), and the circle indicates the measurement range (150 km) of the BSL radar. The gray scales account for the height of topography.

Table 1. Characteristics of the S-band dual-polarization radar at Mt. Bisul (BSL).

Parameter	Value
Frequency (wavelength)	2785 GHz (10 cm, S-band)
Location	$35^\circ 41' 38''$ N, $128^\circ 32' 6''$ E
Altitude	1085 m
Beam width	0.95°
Gate spacing	125 m
Moments	Filtered Z_H , Unfiltered Z_H , V_r , SW , Z_{DR} , ρ_{HV} , Φ_{DP} , K_{DP}
Elevation angles	-0.5° , 0.0° , 0.5° , 0.8° , 1.2° , 1.6°

2DVD instrument captures the shadows of a falling particle using two horizontal light beams which are transmitted from two orthogonal light sources to the two-line scan cameras and provides various information of precipitation particles such as fall velocity, equivalent volume, spherical diameter, major and minor axes, canting angle, and so on [16]. Detail specification is shown in Table 2. These drops information can be contaminated by mismatching of drops in the image processing, which integrates information received from two line-scan cameras [17]. In the case of raindrops,

the mismatched particles can be identified by comparing observed fall velocity (V) with calculated fall velocity (V_A) with the following predefined relationship [18].

$$V_A = 9.65 - 10.3 \exp(-0.6D) \quad (1)$$

Here, the D indicates the diameter of raindrops. The observed drops are eliminated when the difference of the observed fall velocity and calculated fall velocity (V_A) is larger than 40% [16].

Table 2. Specification of two-dimensional video disdrometer (2DVD).

Parameter	Specification
Horizontal resolution	Better than 0.18 mm
Vertical resolution	Better than 0.2 mm for vertical velocity < 10 ms ⁻¹
Vertical velocity accuracy	Better than 4 % for vertical velocity < 10 ms ⁻¹
Rain rate compared to tipping bucket	Differences typically < 10%
Sampling area	100×100 mm ²
Power consumption	Approx. 300 W (outdoor unit + indoor user terminal w/o wind sensor)
Mains voltage	100 – 240 V, 50/60 Hz
Temperature range	–20 – 50 °C
Diameter range	0.0 – 10.25 mm (41 channels)
Physical dimension	850 × 850 × 850 (200) mm
Weight	Approx. 80 kg

The 1-min DSD is then calculated from the velocity filtered drops. The discontinuity check and 3-min moving average are performed to reduce the variation caused by measurement noise. The 22,435 of 1-min DSDs from May 2014 to October 2015 in Jinchun are used to derive the theoretical relationship between dual-polarization variables and microphysical parameters (black lines in Figure 2). The maximum values of rainfall rate, Z_H , and Z_{DR} were 100 mmh⁻¹, 53 dBZ, and 2.5 dB. The 12,945 of 1-min DSDs during 2012 observed in KNU are used to verify retrieved characteristic DSD parameters from the dual-polarimetric radar (blue lines in Figure 2). The maximum rainfall intensity is similar to the Jinchun data set that is used to derive the relationship. However, the maximum reflectivity and differential reflectivity are higher than the Jinchun data set (max. Z_H = 55 dBZ and max. Z_{DR} = 2.8 dB). Both data sets cover various precipitation events. In particular, the Jinchun data set is from about 48 rain events that include wide-spread stratiform rain, frontal precipitation, stationary front (“Changma front”), mesoscale convective precipitation, isolated convection, and typhoon events.

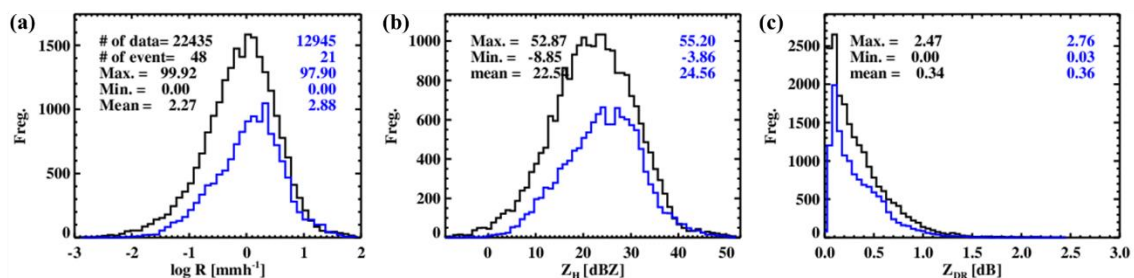


Figure 2. Histogram of (a) rainfall rate, (b) Z_H , (c) Z_{DR} calculated from 2DVD. The data set at the Jinchun site (black lines) is used to derive the retrieval equations, and that at the KNU site (blue lines) is for verifying radar retrieved DSD parameters.

The KNU data set used for evaluation of radar retrieval parameters is composed for the 11 rain events shown in Figure 3. The Z_H plan position indicators (PPIs) at 0.8° elevation angle are shown for each case. The last two events (28 August. and 30 August. 2012) are related to nearby typhoons. The five cases (30 June, 06 July, 11 July, 22 August., and 23 August. 2012) had stationary fronts passing over Korean peninsula. The other cases are linked with troughs and local heating. As shown in Figure 2, the verification data showed heavier rainfall intensity and stronger Z_H than that of the Jinchun site. The mean value of rainfall intensity and Z_H at KNU is larger than that of the Jinchun site.

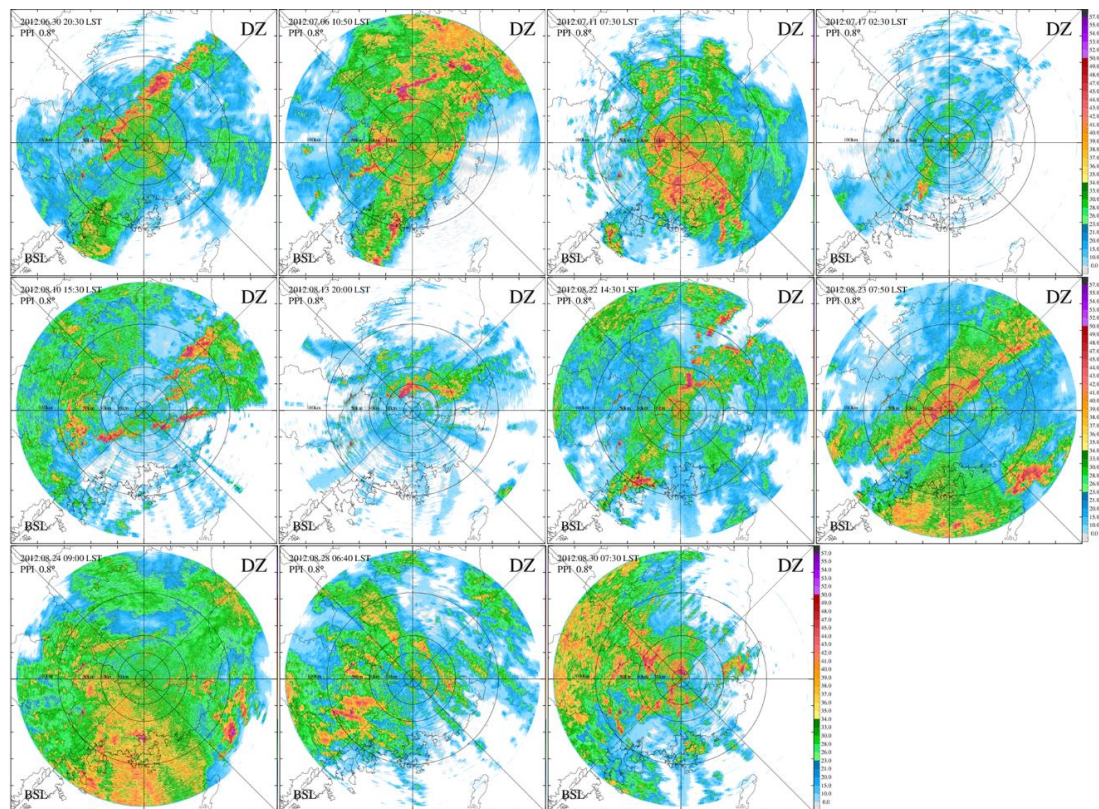


Figure 3. Plan position indicators (PPIs) of radar reflectivity for 11 rain events used for verifying retrieved parameters.

3. Methodology

The relationships between polarimetric variables and microphysical parameters are derived with DSDs obtained from 2DVD. The polarimetric variables are simulated from the T-matrix scattering simulation with 1-min DSDs. The generalized characteristic DSD parameters are calculated from two moments of DSDs. The empirical relationships are then derived with the generalized DSD parameters and simulated radar variables. The details are described in the following sections.

3.1. Simulation of Dual-Polarization Parameters

The polarimetric variables (Z_H , Z_{DR}) are calculated with measured drop size distributions based on the T-matrix method [19,20] with assumptions in Table 3. The frequency of 2.79GHz of BSL radar (S-band) and the dielectric constant of water [21] at an environment temperature of 10°C are assumed. The canting effect caused by tumbling and oscillation of falling raindrops is considered as the Gaussian distribution with the mean canting angle of 0° and the standard deviation of 10° . The axis ratio of the oblate spheroid drop was suggested by many previous studies [22–24]. The axis ratio of the equi-volumetric sphere diameter (D_{eq} in mm) from [25] is used in the present study. The drop shape

was measured by a 2DVD from the 80 m fall experiments [19]. Ref. [25] suggested the following setup: the axis ratio of [17] for $D_{eq} > 1.5$ mm, and [26] for drops smaller than 1.5 mm.

$$\begin{aligned} \frac{b}{a} &= 1 \quad \text{when } D_{eq} \leq 0.7 \text{ mm} \\ \frac{b}{a} &= 1.173 - 0.5165 \times D_{eq} + 0.4698 \times D_{eq}^2 - 0.1317 \times D_{eq}^3 - 8.5 \times 10^{-3} D_{eq}^4 \\ &\quad \text{when } 0.7 < D_{eq} \leq 1.5 \text{ mm} \\ \frac{b}{a} &= 1.065 - 6.25 \times 10^{-2} D_{eq} - 3.99 \times 10^{-3} D_{eq}^2 + 7.66 \times 10^{-4} D_{eq}^3 - 4.095 \times 10^{-5} D_{eq}^4 \\ &\quad \text{when } D_{eq} > 1.5 \text{ mm} \end{aligned} \tag{2}$$

Table 3. Assumption of T-matrix scattering simulation.

Condition	Assumption
Wavelength	10 cm (2.785GHz)
Temperature	10°C
Radar elevation angle	0°
Mean canting angle	0°
Standard deviation of canting angle	10°
Drop shape formulas	Thurai et al. (2007)

3.2. Calculation of Generalized DSD Parameters

Scaling normalization that uses one or two moments of the DSD as a scaling parameter has been used for compact representation of DSD [3,27]. Double-moment normalization uses two moments (i -th moment and j-th moment) as scaling parameters of the normalization as the following equation:

$$N(D) = M_i^{\frac{i+1}{j-i}} M_j^{\frac{j+1}{i-j}} h(x_2), \tag{3}$$

where $h(x_2)$ is the “double-moment normalized” DSD function which is less sensitive to variation of DSD. The normalized diameter (x_2) is $DM_i^{\frac{1}{j-i}} M_j^{\frac{-1}{j-i}}$. The normalization parameters of number concentration and diameter are defined as N_0' and as D_m' , respectively.

$$N_0' = M_i^{\frac{i+1}{j-i}} M_j^{\frac{j+1}{i-j}}, \tag{4}$$

$$D_m' = M_i^{\frac{1}{j-i}} M_j^{\frac{-1}{j-i}} \tag{5}$$

where D_m' [mm] is the generalized characteristic diameter and N_0' [$m^{-3}mm^{-1}$] is the generalized characteristic number concentration. If we take 3rd and 4th moments (i=3 and j=4) as normalization parameters, the D_m' and N_0' are defined as the following equation;

$$N_0' = M_3^5 / M_4^4 \tag{6}$$

$$D_m' = M_4 / M_3 = D_m \tag{7}$$

The definition of D_m' is the same as D_m (mass-weighted mean diameter in mm) in [2]. The N_0' represents the intercept parameter that is approximated with two moments. The choice of two moments depends on the two aspects: (1) Better representation of DSDs and instrumental uncertainty in measuring DSDs. (2) One lower (2nd~3rd) and one higher (6th~7th) moments are desired for the better representation of DSDs. On the other hand, the 2DVD suffers from instrumental uncertainty, in particular, measuring smaller sizes, thus leading to high uncertainty in lower moments [28,29].

Ref. [30] showed that the accuracy of R from 2DVD is the best among different disdrometers with 4 min integration time. However, this is not true in Z due to small sampling volume [30]. Thus, the choice of 3rd and 4th moments is rather a practical approach by considering the data set from which the retrieval relationships are derived.

The empirical relationships are derived with simulated radar variables and calculated microphysical parameters. The microphysical parameters, total number concentration (N_T), and median volume diameter (D_0) were expressed as a polynomial fit in terms of radar measurements [11,12]. The relationships in this study also consists of a polynomial function of Z_{dr} , and the generalized characteristic DSD parameters are normalized with Z_H .

$$\log_{10}(N_0'/Z_h) = a_1 + a_2 Z_{dr} + a_3 Z_{dr}^2 + a_4 Z_{dr}^3, \quad (8)$$

$$D_m/(Z_h)^{b_5} = b_1 + b_2 Z_{dr} + b_3 Z_{dr}^2 + b_4 Z_{dr}^3, \quad (9)$$

where the Z_h and Z_{dr} are a linear scale of Z_H and Z_{DR} , respectively. The coefficients were derived from the calculated N_0' and D_m and simulated radar variables from 22,435 DSDs from the Jinchun site.

4. Accuracy Evaluations of Generalized DSD Parameters

4.1. Characteristics of Generalized DSD Parameters

The generalized DSD parameters calculated from the verification data set are distributed from 0.37 to 3.33 mm for D_m and from 0.43 to 13,804 $\text{m}^{-3}\text{mm}^{-1}$ for N_0' (Figure 4). Ref. [13] investigated the average values of $\log N_W$ and D_m for different climate regions ($D_m \sim 1.5\text{mm}$, $\log N_W \sim 3.25$ in stratiform rain, $D_m \sim 1.75\text{mm}$, $\log N_W \sim 4.25$ in maritime convective rain, and $D_m \sim 2.5\text{mm}$, $\log N_W \sim 3.25$ in continental convective rain). The mean values of D_m and $\log N_0'$ are within the stratiform rain range in [13]. The vertical dashed line in Figure 4b is calculated from Marshal-Palmer (MP) distribution ($\log N_0' = 2.27\text{m}^{-3}\text{mm}^{-1}$, [1]). The mode and mean value are smaller than those of the M-P in this data set. There are second peaks in smaller D_m' ($= 0.5\text{mm}$) and higher $\log N_0'$ ($= 3.3$) that represent drizzle mode.

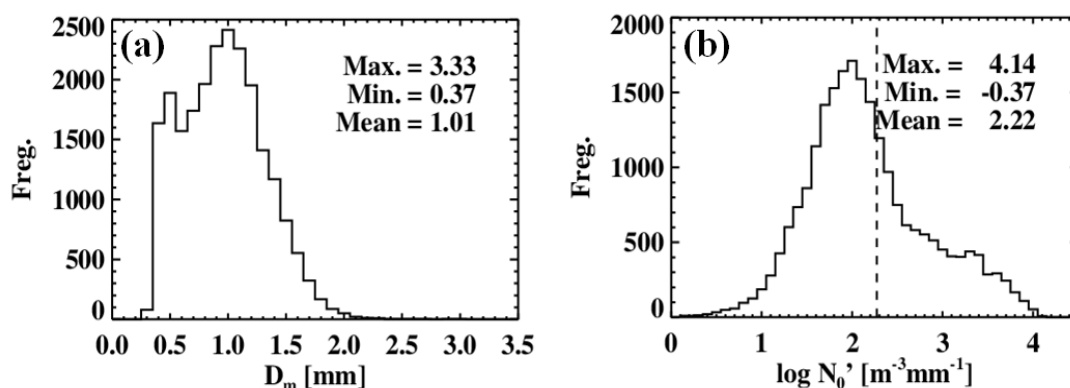


Figure 4. Histogram of (a) mass weighted mean diameter (D_m) and (b) generalized characteristic number concentration (N_0') derived from the verification data set which is composed of 11 rain events (12,945 1-min DSDs). Dashed line indicates N_0' calculated from MP distribution ($\sim 2.27\text{m}^{-3}\text{mm}^{-1}$).

4.2. Relationships between Dual-Polarization Variables and Generalized DSD Parameters

The Z_{DR} shows a good correlation with N_0' and D_m normalized with a linear scale of Z_H (Figure 5). The D_m ($\log N_0'$) monotonically increases (decreases) with the Z_{DR} . The Z_{DR} larger than 0.2dB is used in the regression analysis. The relationships are derived from the third-order polynomial regression.

$$\log_{10}(N_0'/Z_h) = 10^2(0.79 - 1.69Z_{dr} + 1.17 Z_{dr}^2 - 0.28 Z_{dr}^3), \quad (10)$$

$$D_m / (Z_h)^{0.027} = -19.47 + 43.26 Z_{dr} - 30.47 Z_{dr}^2 + 7.33 Z_{dr}^3, \quad (11)$$

where Z_h and Z_{dr} are linear scale of Z_H and Z_{DR} . These equations are used to retrieve the N_0' and D_m .

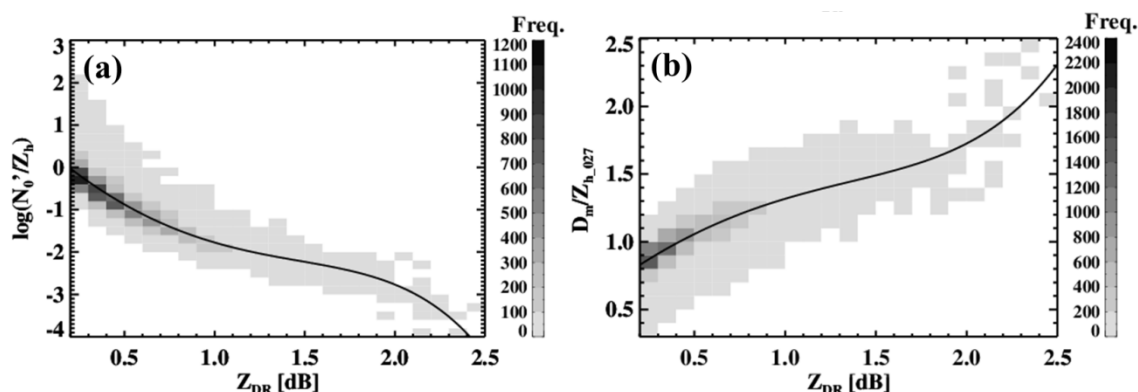


Figure 5. Frequency distribution of Z_{DR} and (a) generalized number concentration ($\log N_0'$) normalized with linear scale of reflectivity (Z_h), and (b) mass-weighted diameter (D_m) normalized with $Z_h^{0.027}$ ($= Z_{h_027}$). Solid lines are polynomial fitting lines.

Theoretical accuracy is evaluated with the same data set measured in the Jinchun. This accuracy should be considered as a theoretical limit in this retrieval method because of the variability of DSD. In general, both N_0' and D_m show high frequency in the one-to-one line, indicating a good accuracy generally (Figure 6). The correlation (standard deviation, SD) is pretty high (smaller), 0.84 (0.26) for $\log N_0'$ and 0.90 (0.11) for D_m . The percentage error (normalized SD, NSD) of $\log N_0'$ and D_m is about 21% and 19%, respectively. The $\log N_0'$ shows slightly larger scatters (Figure 6a). The variation of estimated $\log N_0'$ is more sensitive to Z_{DR} when the reflectivity less 25dBZ. The $\log N_0'$ is varied about $1.0 \text{ m}^{-3}\text{mm}^{-1}$ at 25 dBZ, and $0.75 \text{ m}^{-3}\text{mm}^{-1}$ at 35 dBZ (not shown).

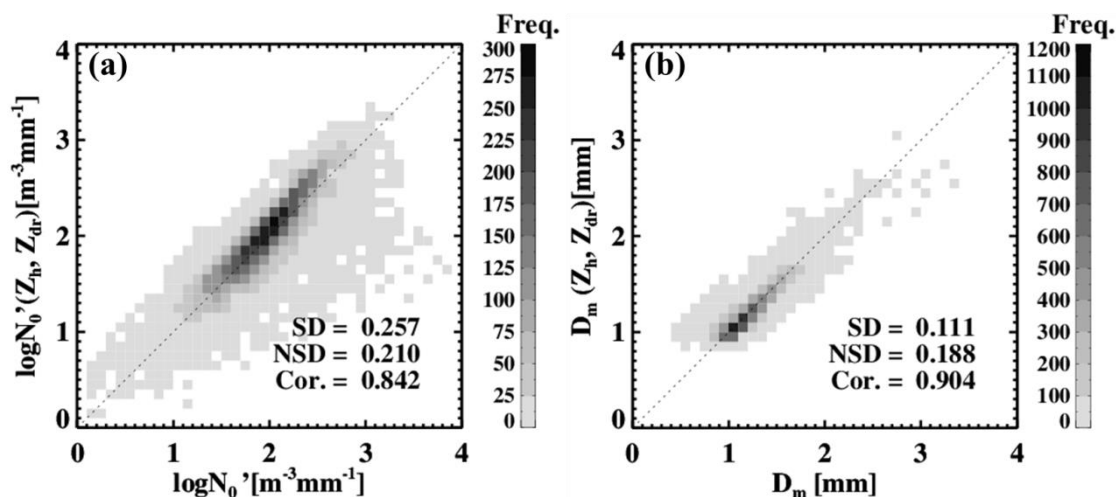


Figure 6. Scatterplots of retrieved (Y values) and calculated (X values) (a) generalized number concentration ($\log N_0'$) and (b) mass-weighted diameter (D_m).

The normalized standard deviation (NSD) is calculated as a function of $\log N_0'$ and D_m with intervals of 0.1 mm, and $0.1 \text{ m}^{-3}\text{mm}^{-1}$, respectively (Figure 7). The dotted line is the number of data (n) within an interval. The NSDs are in the range of 0.09 to 0.20 for $\log N_0'$ and of 0.07 to 0.11 for D_m when $n > 10$. The NSDs are similar to the values suggested in [6] that showed the range of 0.08 to 0.23 for $\log N_0'$ and 0.05 to 0.18 for D_m ([6] used $\log N_W$ instead of $\log N_0'$). Thus, we converted it with the equation $\log N_W = \log N_0' + \log 4!/\Gamma(4)$.

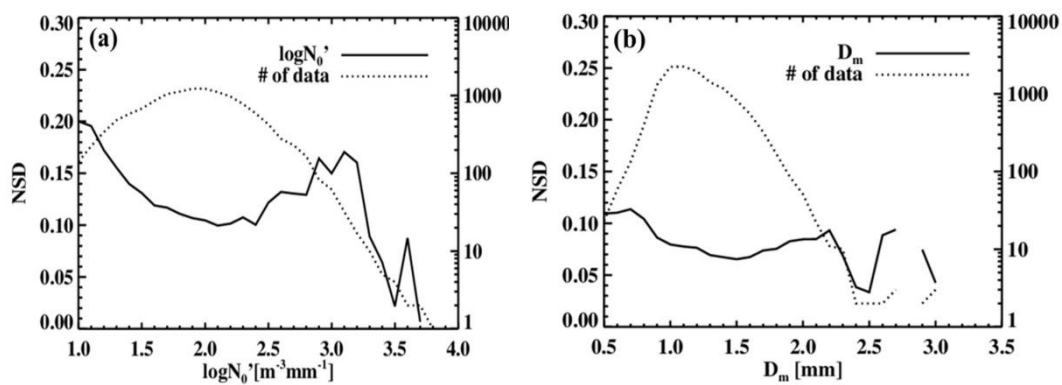


Figure 7. Normalized standard deviation (NSD) of (a) generalized number concentration ($\log N_0'$) and (b) mass-weighted diameter (D_m). Solid line indicates the values of NSD and dotted line indicates the number of data.

4.3. Evaluation of Retrieved Generalized DSD Parameters

A total of 11 rainfall cases (Table 3) during the summer season in 2012 are used to verify the retrieved generalized DSD parameters from the BSL radar. To reduce the effects of measurement noise and the contamination of non-meteorological echoes, the Z_H and Z_{DR} are only selected at the gates with a cross-correlation coefficient greater than 0.95 and they are then averaged in an area of 3° and 1.375 km in azimuthal and radial directions, respectively ($\sim 2 \text{ km}^2$). The measured Z_H and Z_{DR} are calibrated with 2DVD. The generalized DSD parameters of 2DVD are averaged every 5 min based on the radar measurement interval.

The scatterplot of retrieved values from the radar and calculated from measured DSDs are shown in Figure 8 for the 11 rainfall cases, and Table 4 shows the error statistics (correlation coefficient, SD, and bias) of retrieved D_m and $\log N_0'$. The bias is almost negligible in both retrieved D_m and $\log N_0'$. The retrieved D_m was well correlated with D_m calculated from 2DVD with the overall correlation of 0.76 (case correlation of 0.56 to 0.84 shown in Table 4), whereas $\log N_0'$ relatively less correlated with that of 0.39 (case correlation of 0.10 to 0.58). The SDs of D_m and $\log N_0'$ are about 0.19 and 0.46. In general, the retrieval accuracy is quite high for D_m with a little larger error than the theoretical error of $\text{SD} = 0.11$. However, the accuracy of $\log N_0'$ is low as shown by the large scatter in Figure 8b. The $\log N_0'$ shows overestimate at $\log N_0' > 2.0 \text{ m}^{-3} \text{ mm}^{-1}$. The SD of retrieved $\log N_0'$ is close to the double of the theoretical value of 0.26. The individual cases show comparable results.

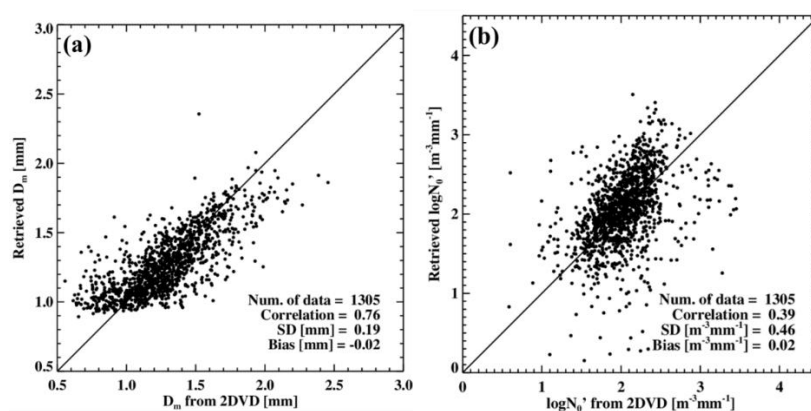


Figure 8. Scatterplots of (a) D_m and (b) $\log N_0'$ retrieved from the BSL radar measurement for the 11 rainfall events during the summer season in 2012.

Table 4. Error statistics of retrieved DSD parameters validated with observed DSDs at the KNU site.

Case	Number of Data	D_m			$\log N_0'$		
		Correlation	SD	Bias	Correlation	SD	Bias
30 Jun.	178	0.74	0.16	−0.02	0.48	0.41	0.04
06 Jul.	52	0.58	0.22	−0.10	0.22	0.64	0.24
11 Jul.	34	0.56	0.16	0.04	0.58	0.37	−0.03
17 Jul.	74	0.72	0.22	−0.05	0.10	0.59	0.06
10 Aug.	29	0.76	0.17	−0.05	0.34	0.27	0.02
13 Aug.	94	0.77	0.23	−0.03	0.25	0.62	0.06
22 Aug.	94	0.84	0.21	−0.05	0.56	0.43	0.09
23 Aug.	331	0.79	0.16	−0.02	0.45	0.38	0.05
24 Aug.	182	0.65	0.12	−0.01	0.41	0.30	0.03
28 Aug.	186	0.56	0.21	0.03	0.24	0.47	−0.08
30 Aug.	51	0.59	0.24	0.06	0.18	0.78	−0.30

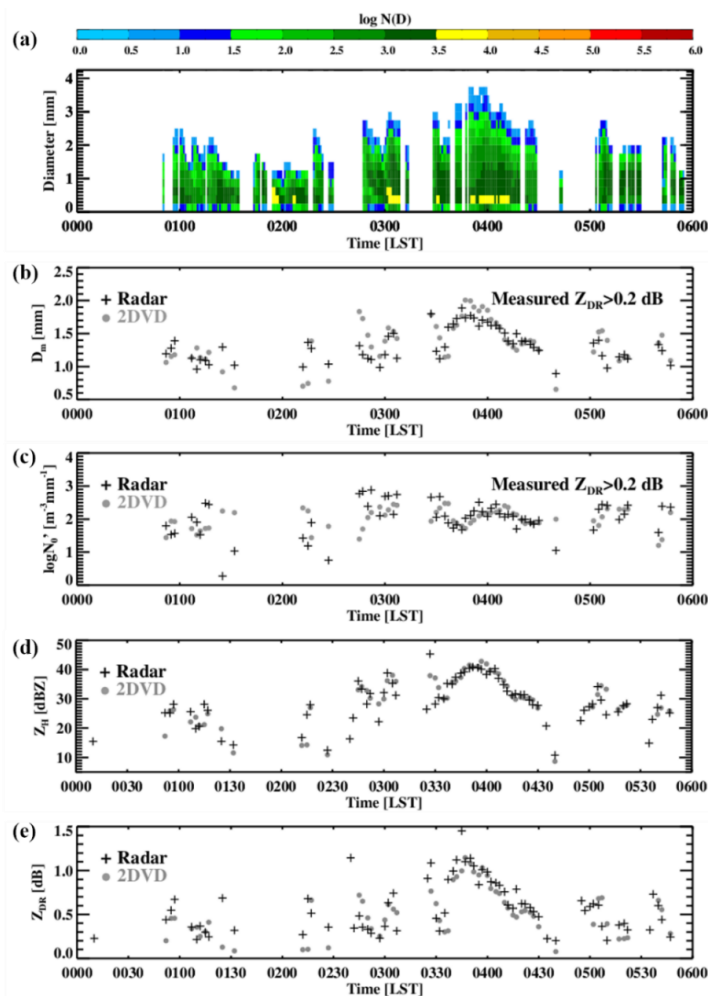


Figure 9. Timeseries of (a) drop size distributions from 2DVD at the KNU site, (b) D_m , (c) $\log N_0'$, (d) reflectivity (Z_H), and (e) differential reflectivity (Z_{DR}) on 17 July 2012. The plus (+) and circles (●) symbols indicate the retrieved values from the BSL radar and the calculated values from 2DVD.

The time series of the retrieved values from the BSL radar and calculated values from 2DVD are shown in Figure 9 to investigate the low accuracy of the retrieved $\log N_0'$ for the case of 17 July 2012 that has the lowest correlation. The retrieved values are well-matched with the calculated values during 0330 LST to 0430 LST when Z_H and, in particular, Z_{DR} are larger, and the rain is continuous. A significant discrepancy (Figure 9d,e) is shown in Z_H and Z_{DR} when Z_H is low. This discrepancy between BSL radar and 2DVD results in a significant difference in $\log N_0'$, subsequently lower correlation. The $\log N_0'$ shows overestimation at $\log N_0'$ larger than $2.0 \text{ m}^{-3} \text{ mm}^{-1}$. The large scatter of $\log N_0'$ are caused by the difference between observed Z_{DR} from radar and 2DVD likely because of the measurement height difference (radar measurement at higher than 1.1 km), measurement noise, and sampling difference.

5. Microphysical Properties of an MCS Case: 14 September 2013

Mesoscale convective systems (MCSs) that include mesoscale convective complexes (MCCs), tropical cyclones, and squall lines are the complex of thunderstorms that involves a well-organized convective region [31–34]. Their spatial dimension can reach hundreds to a thousand kilometers, and their life span can be up to 24 h [35]. Among MCSs, the squall lines are characterized by a strong convection region with strong upward motions at a leading edge and a trailing stratiform region. The strong updraft in the leading edge generates the abundant supercooled droplet, and the vertically developed deep convective systems promote the frequent collision-coalescence process. The well-developed leading edge is usually followed by extensive trailing stratiform regions with relatively weaker rainfall. In this section, the microphysical characteristics of the leading edge and stratiform region in MCS are investigated with the generalized DSD parameters that are retrieved from dual-polarization radar.

5.1. Description of Event

Ref. [28] suggested three primary synoptic conditions that produce heavy precipitation events over the Korean peninsula; a passage of low-level troughs or cyclones, south-westerly flow, and extended low-level troughs. The weather chart of 850 hPa isobaric surface at 0900LST 14 September 2013 shows the troughs located northwest of the Korean Peninsula and large-scale convergence along the south-westerly (not shown). The enhanced infrared imagery from the Communication, Ocean, and Meteorological Satellite (COMS) shows vertically well-developed clouds with a top temperature lower than $-50 \text{ }^\circ\text{C}$. The surface observation at an automatic weather station (AWS) nearby the KNU site shows the dramatic change of wind direction from easterly to westerly with the onset of rain (Figure 10). The westerly persisted throughout the precipitation period (blue shaded). The temperature also dropped about $2 \text{ }^\circ\text{C}$ during the raining period. The rainfall intensity showed one dominant peak at 0950LST on 14 September 2013 with maximum 15 min average rainfall intensity of 36 mm h^{-1} .

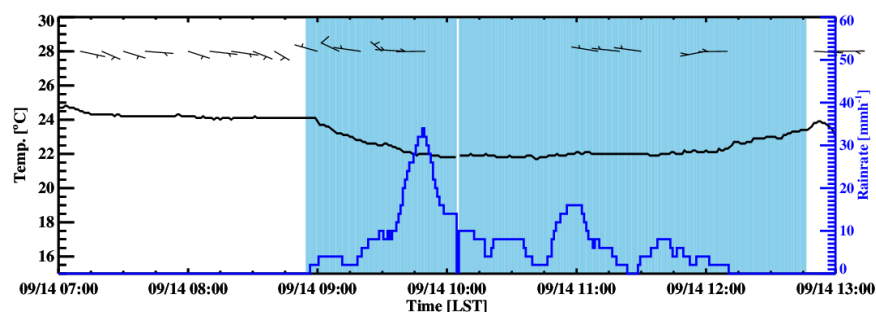


Figure 10. Timeseries of 15-min average rainfall intensity (blue), air temperature (black), and wind speed and direction (wind barbs at the top of figure) at automatic weather station (AWS) located at 1.2km southeast from the KNU for the squall line event on 14 September 2013. Wind barbs are marked every 10 min when wind speed is higher than 2.5 knots). The rain gage is a tipping bucket type with a resolution of 0.5 mm. The shading represents the rain periods identified by the rain detector.

Figure 11 presents the time sequence of Z_H images for MCS on 14 September 2013. The MCS is composed of the leading edge extending from southwest to northeast and following a weak and broad stratiform region. The leading edge developed from 0800 LST to 0930LST and passed through the radar from 0930 to 1030LST. The Z_H of leading edge reached 55 dBZ. The leading-edge then dissipated after 1300LST. The stratiform rain region with relatively low Z_H is followed behind the leading-edge and shows the embedded convection with Z_H higher than 35 dBZ locally.

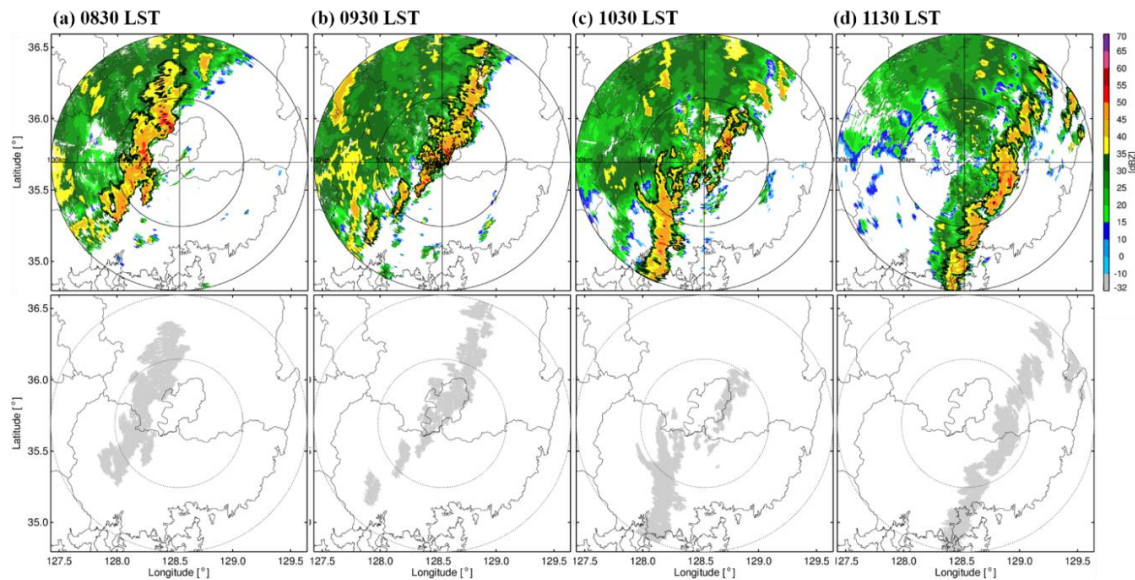


Figure 11. PPIs of (top panel) Z_H and (bottom panel) the classified leading-edge of MCS at 0.8° elevation angle of BSL radar at (a) 0830LST, (b) 0930LST, (c) 1030LST, (d) 1130LST on 14 September 2013. Black solid lines in the upper panel are the boundary of the classified leading edge shown in the bottom panel.

5.2. Classification of MCS

The elevation angle of 0.8° are used to alleviate beam blockage and ground clutter. The quality control (QC) technique based on fuzzy logic [36,37] is applied to remove the ground clutter, chaff echoes, and other non-meteorological echoes. This algorithm is constructed of the optimized membership functions and weights based on the statistical process of polarimetric feature parameters using the long-term data set. The ground clutter, anomalous propagation, chaff, and insects are successfully removed. However, we have noticed some residual of second trip echoes remains near the radar site, causing some error in retrieval of DSD parameters. In addition, the Z_{DR} larger than 0.2dB is used. DSD retrieval is done only in rain regions. The Z_H and Z_{DR} can abruptly change within the bright band. The typical height of the bright band was about 4 km during this rain event. Thus, the radar data are only used within the 100 km range (correspond to 2.5 km altitude of the radar beam center) to avoid the bright band contamination.

The microphysical characteristics and development processes are quite different in the leading edge and extensive trailing stratiform region [15,38,39]. In this study, the leading edge is identified by the fuzzy logic algorithm for storm tracking (FAST) based on radar reflectivity [40]. This algorithm identifies the storm cells using a reflectivity threshold and tracks the cells using the fuzzy logic that utilizes the characteristics of storm cells such as cell motion speed, area change ratio, and axis transformation ratio. First, the two-dimensionally consecutive areas that exceed the reflectivity threshold of 35 dBZ are clustered as a convective cell. This step identifies the storm cells in both the leading edge and trailing stratiform region. The storm average reflectivity is smaller in the embedded cell of the trailing stratiform than that in the leading edge. The cells located at the front of the precipitation system are manually selected and are treated as a single system at the leading edge

with the same characteristics. The lower panel of Figure 11 shows four snapshots of the identified leading edge (grey areas), and the upper panel shows the Z_H PPIs with the identified leading edge in black lines. The leading edge is composed of many storm cells in the front of the precipitation system. The storm cells in trailing regions are excluded and are treated as the trailing stratiform region. As shown in the lower panel, its line shape is well illustrated and tracked. The DSD characteristics of the leading edge are derived from these grey areas. On the other hand, those of the stratiform region are from all areas except for the grey region. Thus, some of the weak echo areas in the leading edge is included in the stratiform region.

5.3. Microphysical Characteristics of MCS Case

The time series of averaged Z_H and Z_{DR} of leading-edge is shown in Figure 12a. The Z_H values of the leading edge are high (up to 43 dBZ) in the earlier period (~0930LST). The Z_H and Z_{DR} are somewhat positively correlated in this period, and Z_{DR} has the maximum value around 0920~0930LST. After this period, both values decrease until 1100LST. The Z_H continuously decreases while Z_{DR} increases. That is, both values are negatively correlated in the period of 1100LST to 1300LST. However, some periods such as 0827LST and 0915LST~1003LST show dramatic change of the averaged Z_H and Z_{DR} in the leading-edge, in particular, unrealistic change of Z_{DR} . Thus, we further investigate the potential causes of this change.

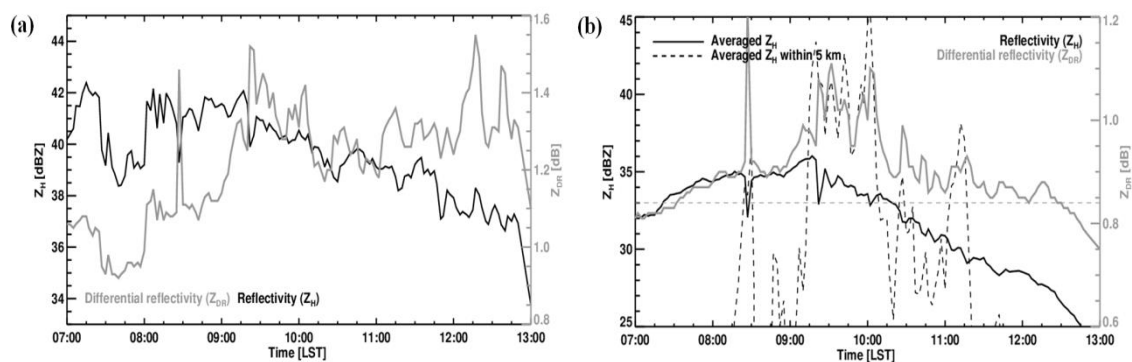


Figure 12. Time series of (a) averaged reflectivity (Z_H , black) and differential reflectivity (Z_{DR} , gray) at the leading-edge and (b) averaged Z_H and Z_{DR} for the entire area (solid line) and the circle area with the radius of 5 km centered to radar site (dashed line). The average is done in dB unit.

The averaged Z_H and Z_{DR} for the entire observation area (including the leading edge and stratiform area) increase until 0930LST and after then, the Z_H decreased rapidly (Figure 12b). On the other hand, the Z_{DR} values largely fluctuate during 0920~1005LST and gently decreases after 1015LST with some fluctuation (gray solid line in Figure 12b). The rapid fluctuation of Z_{DR} is highly correlated with the Z_H around the BSL radar indicated by the average reflectivity values near radar (dashed line). In particular, the sudden increase on Z_{DR} at 0827LST, 0915LST~1003LST, and 1012LST~1120LST is driven by the significant rain over the radar site, caused by significant differential wet radome attenuation. The vertically flowing water shield causes more considerable attenuation in vertical polarization than in horizontal polarization. The wet radome attenuation is also confirmed by the drop of average reflectivity value in the entire area (black solid line in Figure 12b) at 0827LST, 0920LST, 0931LST, and 1000LST. The sudden change of Z_H and Z_{DR} affects the retrieved microphysical parameters (as shown in Figures 13–15). The period of significant rain over the radar site was excluded in the statistical analysis with the threshold of average Z_H near the radar (about 33 dBZ) to avoid so the wet radome attenuation.

Figure 13 shows the time series of the averaged generalized DSD parameters, D_m and $\log N_0'$ in the leading-edge (plus symbol), trailing stratiform (diamond symbol), and overall regions (solid line). Their frequency distribution is also shown in Figures 14 and 15. The sudden change of $\log N_0'$ and D_m

is noticed because of the wet radome attenuation and should be discarded in the analysis afterward. The $\log N_0'$ in the stratiform (left panel in Figure 14) region remains nearly constant or slightly increased (average $\log N_0' \sim 2.2 \text{ m}^{-3} \text{ mm}^{-1}$ in Figure 13a) until 0920LST and shows the temporal fluctuation in 0930~1000LST due to the wet radome attenuation. The $\log N_0'$ in the leading-edge region is nearly constant until 0920LST with a higher average of $2.4 \text{ m}^{-3} \text{ mm}^{-1}$ than the stratiform region. The overall gradual decrease is shown with slightly higher average values but significant fluctuation with time. The D_m (Figure 15a) in the stratiform region is nearly constant (average $D_m \sim 1.3 \text{ mm}$ in Figure 13b) throughout the period. The D_m in the leading edge (Figure 15b) gradually increases with time until 0920LST and remains constant with the average value of 1.8 mm (Figure 13b). The values of D_m are much higher in the leading edge than in the stratiform region.

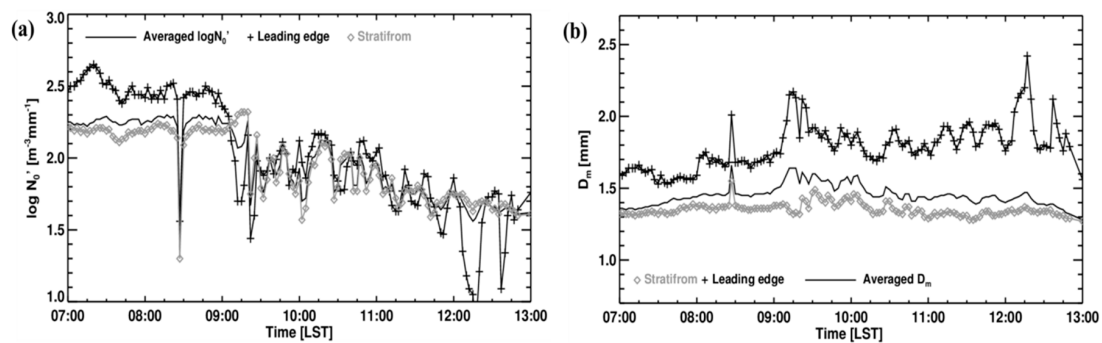


Figure 13. Time series of (a) $\log N_0'$ and (b) D_m averaged for the entire area (black solid line), leading edge (black line with cross symbol), and stratiform area (gray line with diamond symbol).

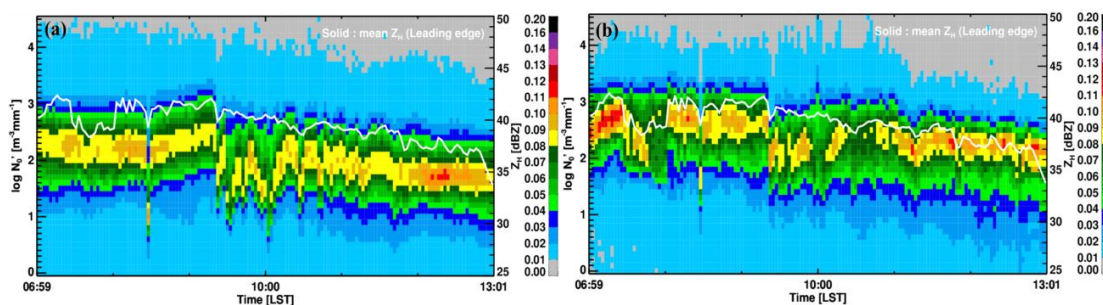


Figure 14. Time series of the frequency of $\log N_0'$ in (a) the trailing stratiform region and (b) the leading-edge region on 14 September 2013. Colors represent the normalized frequency of $\log N_0'$. The white solid line is the mean reflectivity in the leading-edge region.

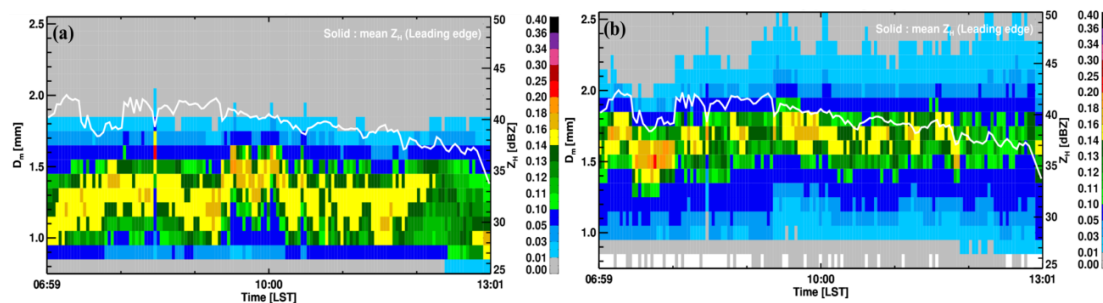


Figure 15. Time series of the frequency of except for D_m in (a) the trailing stratiform region and (b) the leading-edge region on 14 September 2013. Colors represent the normalized frequency of D_m . The white solid line is the mean reflectivity in the leading-edge region.

In summary, the early period in the leading edge shows the most active drop growth by the collision-coalescence process with an abundant new generation of drops. Significant skewness toward

higher $\log N_0'$ is shown in the frequency distribution of $\log N_0'$ in the leading-edge (Figure 14b). That is, the leading is characterized as higher $\log N_0'$ as shown in [15] and [39]. In addition, Lagrangian temporal evolution in this study indicates that the drop growth becomes more active until 0920LST in the leading edge. Furthermore, the new generation of drops becomes less important, and the drop growth by the collision-coalescence remains dominant after 0920LST, as shown by the gradual increases of D_m . However, the collision-coalescence is not the dominant process in the trailing stratiform region as shown by nearly constant D_m (Figure 13b). The new generation of small drops was significant in the early period in the stratiform region. This may be originated by the supply of new ice particles from the leading edge in which the strong updraft prevails during the early period. However, this becomes weaker after 0920LST because of the weakening of overall systems as seen by decreasing of the average Z_H over the entire measurement area (see Figure 12b). The large spread of the frequency distribution of D_m indicates the diversity of precipitation systems within the trailing stratiform region such as weak stratiform rain and embedded convection.

The statistical distribution of the generalized characteristic parameters is investigated for the stratiform region and leading edge in the early (0820LST) and later (1130LST) periods when the Lagrangian temporal evolution is quite different (Figure 16). The D_m is larger in the leading edge with averages of 1.67~1.94 mm than in the stratiform with averages of 1.31~1.37 mm. In particular, the long tail in larger D_m is prominent in the leading edge. The $\log N_0'$ is also larger in the leading edge with average values of 1.68~2.51 $\text{m}^{-3}\text{mm}^{-1}$ than in the stratiform with averages of 1.77~2.19 $\text{m}^{-3}\text{mm}^{-1}$.

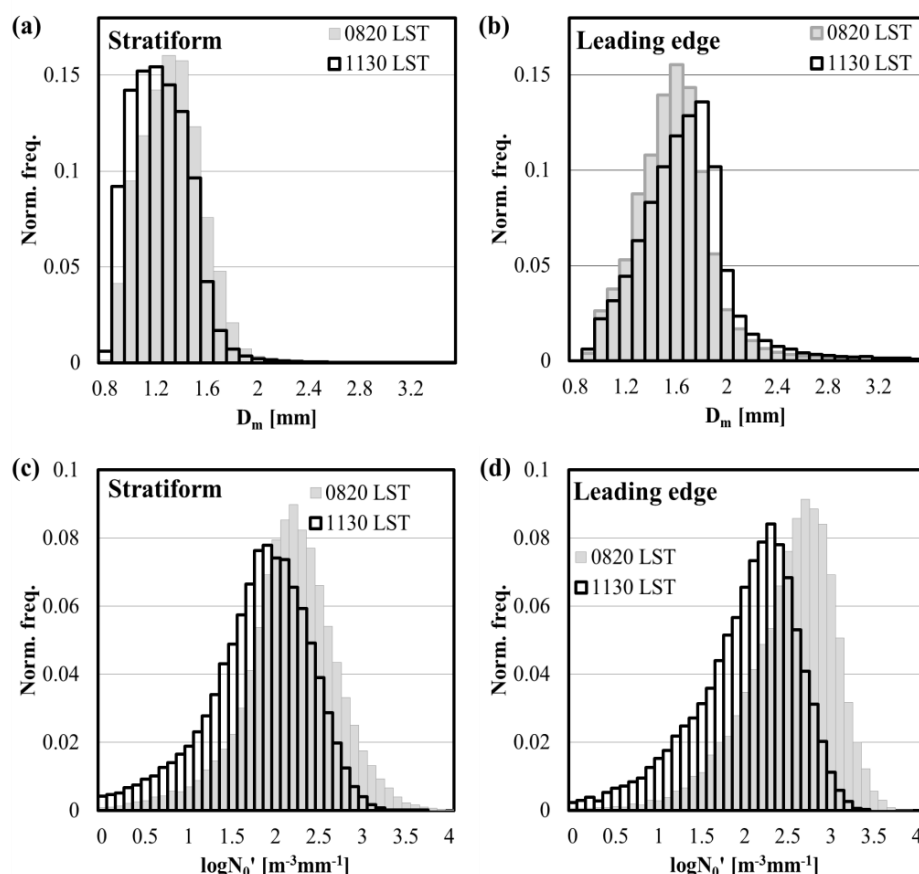


Figure 16. Normalized frequency distribution of (a) D_m and (c) $\log N_0'$ in the stratiform region at 0820 LST (gray vertical bar) and 1130 LST (black vertical bar). The distribution in the leading edge is shown in (b) for D_m and in (d) for $\log N_0'$.

The Lagrangian temporal evolution of $\log N_0'$ (D_m) shows the same trend (opposite trend) in the stratiform and leading-edge regions. That is, the $\log N_0'$ decreases with time in both regions (lower

panel in Figure 16), caused by the significant reduction of the newly generated drops as the precipitation systems weaken. However, the D_m decreases with time in the stratiform region while it becomes larger with time in the leading edge, indicating the drop growth by the dominant collision-coalescence process in the leading-edge throughout the period.

As explained in Section 5.2, the cells in the leading edge are treated as the same precipitation system in the same development stage. In fact, all cells are unlikely in the same stage. This complicates the interpretation of derived DSD parameters. Thus, the results should be understood as the evolution of the cell complex rather than that of individual cells.

6. Conclusions

The temporal evolution of microphysical characteristics of precipitation systems can be investigated in high temporal and spatial resolution and in Lagrangian framework by dual-polarimetric radar measurement in wide areas. We derived the relationships between differential reflectivity and generalized DSD parameters normalized by radar reflectivity derived from DSDs. The dual-polarization radar variables and generalized DSD parameters (general number concentration, $N_{0'}$, and generalized mean diameter, D_m) were derived by using the 2-D video distrometer data observed during 10 months in the Jinchun site. These relationships were applied to 11 rain events to retrieve $N_{0'}$ and D_m from the BSL dual-polarimetric radar, and the retrieved parameters were then verified by DSDs observed from a 2DVD located at 23 km away from the radar. A mesoscale convective system (MCS) on 14 September 2013 was classified into the two regions (the leading edge and trailing stratiform region) by the storm classification algorithm [39]. The microphysical characteristics in the two regions were then investigated with retrieved parameters from the radar in the Lagrangian frame.

The reflectivity (Z_H) and differential reflectivity (Z_{DR}) were simulated from DSDs with the T-matrix calculation, and the $N_{0'}$ and D_m are derived from the 3rd and 4th moments of DSDs with the assumption on the scaling normalization of DSDs. Then, the $N_{0'}$ and D_m normalized by Z_H were fitted as polynomial functions of Z_{DR} , and these fitted polynomial functions were used to retrieve $N_{0'}$ and D_m from the dual-polarimetric measurement. First, we calculated the theoretical accuracy of this retrieval method due to the variability of DSDs. The normalized standard deviations (NSD) of retrieved DSD parameters were in the range of 0.07 to 0.11 (average SD of 0.11) for D_m and of 0.09 to 0.2 (average SD of 0.26) for $\log N_{0'}$ that were quite comparable with the results in [6].

However, the accuracy deteriorated when applied to the actual radar measurement. The retrieval accuracy of D_m ($\log N_{0'}$) was quite high (low). The overall correlation of D_m ($\log N_{0'}$) for 11 rain events was 0.76 (0.39). The SDs of D_m and $\log N_{0'}$ were about 0.19 and 0.46. A significant overestimation was noticed at $\log N_{0'} > 2.0 \text{ m}^{-3}\text{mm}^{-1}$. This overall low accuracy in $\log N_{0'}$ was attributed to the significant discrepancy of Z_H and Z_{DR} from radar measurement and 2DVD, in particular when Z_H and Z_{DR} are low. In addition, the $\log N_{0'}$ is an intercept parameter that relies on the lower moments. However, the $\log N_{0'}$ was derived from the higher moment (Z_H) and the ratio of higher moments (Z_{DR}). Subsequently, the small measurement errors either in Z_H and Z_{DR} severely affect the retrieval accuracy of the $\log N_{0'}$. Thus, the measurement or estimation of lower moments is key to improve retrieval accuracy and should be investigated further.

The temporal evolution of microphysical characteristics was investigated in the MCS system using retrieved values of $N_{0'}$ and D_m . The leading edge dominated by strong updraft showed broad DSD spectra with higher number concentration and larger characteristic diameter. The frequency distribution of $\log N_{0'}$ skewed negatively (tail in low concentration and peak toward higher $\log N_{0'}$). The increase of D_m is noticeable in the leading edge, in particular when the precipitation system grows. This indicates that the drop growth by the collision-coalescence process was dominant in the leading edge throughout the event. In addition, the value of $\log N_{0'}$ ($\sim 2.5 \text{ m}^{-3}\text{mm}^{-1}$) was high and steady in the leading edge for the early period when the system grows. When the system weakens, its value decreases with time. This implies that both the new generation of drops and drop growth by the coalescence was dominant in the early period of the leading-edge. However, when the system weakens,

the new generation of drops becomes less significant while the growth of the drop by collision and coalescence remains.

On the other hand, the value of D_m remains constant throughout the event in the trailing stratiform region. The value of $\log N_0'$ is nearly constant with a similar value of MP when the entire precipitation grows. However, its value decreases with time for the later period, similar to the leading edge. Thus, the collision-coalescence process is less important throughout the event in the trailing stratiform region. The new generation of small drops was important in the early period. This is likely due to the supply of new ice particles from the leading edge. In addition, the frequency distributions of D_m and $\log N_0'$ were broader, indicating the diversity of the precipitation systems as shown by embedded convection within the stratiform region.

The Lagrangian evolution of DSDs can provide an insight into the interaction between the dynamical and microphysical processes. The separation of the leading edge and trailing stratiform is a proxy of classification of the strong updraft and steady weak upward motion. The leading edge is typically characterized by the strong updraft in the early developing period, and the strength of the updraft becomes weak as the system approaches the decaying period. The Lagrangian evolution of $\log N_0'$ and D_m reflects this dynamical aspect. The Lagrangian temporal evolution of $\log N_0'$ showed the same trend in the leading-edge and trailing stratiform region. That is, the peak of the distribution shifted to smaller values. This indicates that its value is controlled by the growing and weakening of the precipitation system. However, the value of D_m showed the opposite trend. That is, its value decreases with time in the trailing stratiform and vice versa in the leading-edge. Thus, we can conclude that the drop growth in the leading-edge is controlled by the collision-coalescence process for the entire event. However, the new generation of small drops is important in the drop growth in the trailing stratiform region shown in the early period.

In this study, we did not attempt to retrieve the functional form of normalized DSDs. However, the function may vary in smaller temporal and spatial scales, although it is nearly constant in a climatological sense. It is trivial that some microphysical processes, such as evaporation, will change the function of normalized DSDs. However, the change of the function becomes less significant in the normalized DSDs than that in the DSDs since the significant variation is somewhat contained in the generalized characteristic parameters. Nevertheless, exploration on the function of the normalized DSDs further merits a more detailed understanding of the microphysical evolution of precipitation systems.

Author Contributions: This work was possible by significant contribution from all authors. Conceptualization, G.L. and S.K.; methodology, S.K., S.-H.J., and G.L.; software, S.K. and S.-H.J.; validation, S.K., and S.-H.J.; formal analysis, S.K. and G.L.; investigation, S.K. and G.L.; writing—original draft preparation, S.K.; writing—review and editing, G.L. and S.-H.J.; visualization, S.K.; supervision, G.L.; funding acquisition, G.L. All authors have read and agreed to the published version of the manuscript.

Funding: This research is supported by “Development and application of cross governmental dual-pol radar harmonization (WRC-2013-A-1)” project of the Weather Radar Center, Korea Meteorological Administration.

Acknowledgments: This paper is based on the part of Soohyun Kwon’s thesis.

Conflicts of Interest: The authors declare no conflict of interest.

References

1. Marshall, J.S.; Palmer, W.M. The size distribution of raindrops. *J. Meteor.* **1948**, *5*, 165–166. [[CrossRef](#)]
2. Testud, J.; Oury, S.; Amayenc, P. The concept of “normalized” distribution to describe raindrop spectra: A tool for hydrometeor remote sensing. *Phys. Chem. Earth Part. B Hydrol. Ocean. Atmos.* **2000**, *25*, 897–902. [[CrossRef](#)]
3. Lee, G.W.; Zawadzki, I.; Szyrmer, W.; Sempere-Torres, D.; Uijlenhoet, R. A general approach to double-moment normalization of drop size distributions. *J. Appl. Meteorol.* **2004**, *43*, 264–281. [[CrossRef](#)]
4. Brandes, E.A.; Zhang, G.; Vivekanandan, J. An Evaluation of a Drop Distribution–Based Polarimetric Radar Rainfall Estimator. *J. Appl. Meteorol.* **2003**, *42*, 652–660. [[CrossRef](#)]

5. Cao, Q.; Zhang, G.; Brandes, E.A.; Schuur, T.J. Polarimetric radar rain estimation through retrieval of drop size distribution using a bayesian approach. *J. Appl. Meteorol. Climatol.* **2010**, *49*, 973–990.
6. Gorgucci, E.; Chandrasekar, V.; Bringi, V.N.; Scarchilli, G. Estimation of Raindrop Size Distribution Parameters from Polarimetric Radar Measurements. *J. Atmos. Sci.* **2002**, *59*, 2373–2384. [[CrossRef](#)]
7. Vulpiani, G.; Marzano, F.S.; Chandrasekar, V.; Berne, A.; Uijlenhoet, R. Polarimetric weather radar retrieval of raindrop size distribution by means of a regularized artificial neural network. *IEEE Trans. Geosci. Remote Sens.* **2006**, *44*, 3262–3274. [[CrossRef](#)]
8. Yoshikawa, E.; Chandrasekar, V.; Ushio, T.; Matsuda, T. A Bayesian approach for integrated raindrop size distribution (DSD) retrieval on an X-band dual-polarization radar network. *J. Atmos. Ocean. Technol.* **2016**, *33*, 377–389. [[CrossRef](#)]
9. Zhang, G.; Vivekanandan, J.; Brandes, E.A. A method for estimating rain rate and drop size distribution from polarimetric radar measurements. *IEEE Trans. Geosci. Remote Sens.* **2001**, *39*, 830–841. [[CrossRef](#)]
10. Gorgucci, E.; Scarchilli, G.; Chandrasekar, V.; Bringi, V.N. Measurement of mean raindrop shape from polarimetric radar observations. *J. Atmos. Sci.* **2000**, *57*, 3406–3413. [[CrossRef](#)]
11. Brandes, E.A.; Zhang, G.; Vivekanandan, J. Drop size distribution retrieval with polarimetric radar: Model and application. *J. Appl. Meteorol.* **2004**, *43*, 461–475. [[CrossRef](#)]
12. Cao, Q.; Zhang, G.; Brandes, E.A.; Schuur, T.; Ryzhkov, A.V.; Ikeda, K. Analysis of video disdrometer and polarimetric radar data to characterize rain microphysics in Oklahoma. *J. Appl. Meteorol. Climatol.* **2008**, *47*, 2238–2255. [[CrossRef](#)]
13. Bringi, V.N.; Chandrasekar, V.; Hubbert, J.; Gorgucci, E.; Randeu, W.L.; Schonhuber, M. Raindrop Size Distribution in Different Climatic Regimes from Disdrometer and Dual-Polarized Radar Analysis. *J. Atmos. Sci.* **2003**, *60*, 354–365. [[CrossRef](#)]
14. Chang, W.-Y.; Wang, T.-C.C.; Lin, P.-L. Characteristics of the Raindrop Size Distribution and Drop Shape Relation in Typhoon System in the Western Pacific from the 2D Video Disdrometer and NCU C-Band Polarimetric Radar. *J. Atmos. Ocean. Technol.* **2009**, *26*, 1973–1993. [[CrossRef](#)]
15. Jung, S.-A.; Lee, D.-I.; Jou, B.J.-D.; Uyeda, H. Microphysical Properties of Maritime Squall Line Observed on June 2, 2008 in Taiwan. *J. Meteorol. Soc. Jpn.* **2012**, *90*, 833–850. [[CrossRef](#)]
16. Kruger, A.; Krajewski, W.F. Two-Dimensional Video Disdrometer: A description. *J. Atmos. Ocean. Technol.* **2002**, *19*, 602–617. [[CrossRef](#)]
17. Thurai, M.; Bringi, V.N. Drop axis ratios from a 2D video disdrometer. *J. Atmos. Ocean. Technol.* **2005**, *22*, 966–978. [[CrossRef](#)]
18. Atlas, D.; Srivastava, R.C.; Sekhon, R.S. Doppler radar characteristics of precipitation at vertical incidence. *Rev. Geophys.* **1973**, *11*, 1–35. [[CrossRef](#)]
19. Bringi, V.N.; Chandrasekar, V.; Balakrishnan, N.; Zrnich, D.S. An Examination of Propagation Effects in Rainfall on Radar Measurements at Microwave Frequencies. *J. Atmos. Ocean. Technol.* **1990**, *7*, 829–840. [[CrossRef](#)]
20. Vivekanandan, J.; Adams, W.M.; Bringi, V.N. Rigorous approach to polarimetric radar modeling of hydrometeor orientation distributions. *J. Appl. Meteorol.* **1991**, *30*, 1053–1063. [[CrossRef](#)]
21. Ray, P.S. Broadband complex refractive indices of ice and water. *Appl. Opt.* **1972**, *11*, 1836–1844. [[CrossRef](#)]
22. Beard, K.V.; Chuang, C. A new model for the equilibrium shape of raindrops. *J. Atmos. Sci.* **1987**, *44*, 1509–1524. [[CrossRef](#)]
23. Pruppacher, H.R.; Beard, K.V. A wind tunnel investigation of the internal circulation and shape of water drops falling at terminal velocity in air. *Quart. J. Roy. Meteorol. Soc.* **1970**, *96*, 247–256. [[CrossRef](#)]
24. Brandes, E.A.; Zhang, G.; Vivekanandan, J. Experiments in Rainfall Estimation with a Polarimetric Radar in a Subtropical Environment. *J. Appl. Meteorol.* **2002**, *41*, 674–685. [[CrossRef](#)]
25. Thurai, M.; Huang, G.J.; Bringi, V.N.; Randeu, W.L.; Schonhuber, M. Drop shapes, model comparisons, and calculations of polarimetric radar parameters in rain. *J. Atmos. Ocean. Technol.* **2007**, *24*, 1019–1032. [[CrossRef](#)]
26. Beard, K.V.; Kubesh, R.J. Laboratory measurements of small raindrop distortion. Part 2: Oscillation frequencies and modes. *J. Atmos. Sci.* **1991**, *48*, 2245–2264. [[CrossRef](#)]
27. Torres, D.S.; Porra, J.M.; Creutin, J.D. A general formulation for raindrop size distribution. *J. Appl. Meteorol.* **1994**, *33*, 1494–1502. [[CrossRef](#)]

28. Cao, Q.; Zhang, G. Errors in estimating raindrop size distribution parameters employing disdrometer and simulated raindrop spectra. *J. Appl. Meteorol. Climatol.* **2009**, *48*, 406–425. [[CrossRef](#)]
29. Thurai, M.; Gatlin, P.; Bringi, V.N.; Petersen, W.; Kennedy, P.; Notaroš, B.; Carey, L. Toward completing the raindrop size spectrum: Case studies involving 2D-video disdrometer, droplet spectrometer, and polarimetric radar measurements. *J. Appl. Meteorol. Climatol.* **2017**, *56*, 877–896. [[CrossRef](#)]
30. Chang, W.-Y.; Lee, G.; Jou, B.J.-D.; Lee, W.-C.; Lin, P.-L.; Yu, C.-K. Uncertainty in measured raindrop size distributions from four types of collocated instruments. *Remote Sens.* **2020**, *12*, 1167. [[CrossRef](#)]
31. Lee, T.Y.; Kim, Y. Heavy Precipitation systems over the Korean peninsula and their classification. *J. Korean Meteorol. Soc.* **2007**, *43*, 367–396.
32. Markowski, P.; Richardson, Y. *Mesoscale Meteorology in Midlatitudes*; John Wiley & Sons, Ltd.: Hoboken, NJ, USA, 2010; p. 245.1.
33. Lee, J.-T.; Lee, D.; Shimizu, S.; You, C.-H. Analysis of determinants for an enhanced and long-lasting coastal convective system by means of a case study (26 July 2011). *Adv. Atmos. Sci.* **2019**, *36*, 1327–1339. [[CrossRef](#)]
34. Ke, C.-Y.; Chung, K.-S.; Wang, T.-C.C.; Liou, Y.-C. Analysis of heavy rainfall and barrier-jet evolution during Mei-Yu season using multiple doppler radar retrievals: A case study on 11 June 2012. *Tellus A Dyn. Meteorol. Oceanogr.* **2019**, *71*, 1–21. [[CrossRef](#)]
35. Houze, R.A. Mesoscale convective systems. *Rev. Geophys.* **2004**, *42*, RG4003. [[CrossRef](#)]
36. Cho, Y.H.; Lee, G.W.; Kim, K.E.; Zawadzki, I. Identification and removal of ground echoes and anomalous propagation using the characteristics of radar echoes. *J. Atmos. Oceanic Technol.* **2006**, *23*, 1206–1222. [[CrossRef](#)]
37. Ye, B.; Lee, G.W.; Park, H. Identification and removal of non-meteorological echoes in dual-polarization radar data based on a fuzzy logic algorithm. *Adv. Atmos. Sci.* **2015**, *32*, 1217–1230. [[CrossRef](#)]
38. Chen, G.; Zhao, K.; Wen, L.; Wang, M.; Huang, H.; Wang, M.; Yang, Z.; Zhang, G.; Zhang, P.; Lee, W.-C. Microphysical characteristics of three convective events with intense rainfall observed by polarimetric radar and disdrometer in eastern China. *Remote Sens.* **2019**, *11*, 2004. [[CrossRef](#)]
39. Uijlenhoet, R.; Steiner, M.; Smith, J.A. Variability of raindrop size distributions in a squall line and implications for radar rainfall estimation. *J. Hydrometeor.* **2003**, *4*, 43–61. [[CrossRef](#)]
40. Jung, S.-H.; Lee, G.W. Radar-based cell tracking with fuzzy logic approach. *Meteorol. Appl.* **2015**, *22*, 716–730. [[CrossRef](#)]

